Author Manuscript

Nanoscale structural and emission properties within “Russian Doll”-type InGaN/AlGaN quantum wells

Shaobo Cheng,[1,†] Zewen Wu,[2,3,†] Brian Langelier,[1] Xianghua Kong,[2,*] Toon Coenen,[4] Sangeetha Hari,[4] Yong-Ho Ra,[5,6] Roksana Tonny Rashid,[5] Alexandre Pofelski,[1] Hui Yuan,[1] Xing Li,[7] Zetian Mi,[5,8] Hong Guo,[2] Gianluigi A. Botton[1,9,*]

1. Canadian Centre for Electron Microscopy and Department of Materials Science and Engineering, McMaster University, Main Street West, Hamilton, Ontario, L8S 4M1, Canada
2. Department of Physics, McGill University, 3480 University Street, Montreal, Quebec H3A 0E9, Canada
3. Beijing Key Laboratory of Nanophotonics and Ultrafine Optoelectronic Systems, School of Physics, Beijing Institute of Technology, 5 Zhongguancun South Street, Beijing 100081, China
4. Delmic, Kanaalweg 4, 2628 EB Delft, The Netherlands
5. Department of Electrical and Computer Engineering, McGill University, 3480 University Street, Montreal, Quebec H3A 0E9, Canada
6. Optic & Electronic Component Material Center, Korea Institute of Ceramic Engineering & Technology, Jinju 52851, Republic of Korea
7. School of Physics and Engineering, Zhengzhou University, Daxue Road 75, Zhengzhou, 450052 China
8. Department of Electrical Engineering and Computer Science, University of Michigan, 1301 Beal Avenue, Ann Arbor, MI 48109, USA

This is the author manuscript accepted for publication and has undergone full peer review but has not been through the copyediting, typesetting, pagination and proofreading process, which may lead to differences between this version and the Version of Record. Please cite this article as doi: 10.1002/adom.202000481.

This article is protected by copyright. All rights reserved.

Author Manuscript

9. Canadian Light Source, 44 Innovation Boulevard Saskatoon, Saskatchewan, S7N 2V3, Canada

Corresponding authors

*Email: gbotton@mcmaster.ca

*Email: kongxianghua2012@gmail.com

Keywords: Sub-wavelength materials, transmission electron microscopy, cathodoluminescence, atom probe tomography, strain effects

Abstract

Due to the increasing desire for nanoscale optoelectronic devices with green light emission capability and high efficiency, ternary III-N-based nanorods have been extensively studied. Many efforts have been taken on the planar device configuration, which lead to unavoided defects and strains. With selective-area molecular-beam epitaxy, new “Russian Doll” type InGaN/AlGaN quantum wells (QWs) have been developed, which could largely alleviate this issue. This work combines multiple nanoscale characterization methods and k·p theory calculations so that the crystalline structure, chemical compositions, strain effects, and light emission properties can be quantitatively correlated and understood. The three-dimensional

This article is protected by copyright. All rights reserved.

Author Manuscript

structure and atomic composition of these QWs are retrieved with transmission electron microscopy (TEM) and atom probe tomography (APT) while their green light emission has been demonstrated with room-temperature cathodoluminescence experiments. k·p theory calculations, accounting for the quantitative measured compositions of the nanorods, and with the consideration of strain effects, are used to derive the light emission characteristics that are compared with the local measurements. Thus, the structural properties of the newly designed nanorods are quantitatively characterized and the relationship with their outstanding optical properties are described. This combined approach provides an innovative way for analyzing nano-optical-devices and new strategies for the structure design of light-emitting diodes.

The chemical components of the nanorods, shape effects and strain effects given by this unique “Russian Doll”-type geometry of InGaN/AlGaN quantum wells are quantitatively related with the optical properties. This combined approach reported here provides an innovative way for analyzing nano-optical-devices and new strategies for the structure design of light-emitting diodes.

This article is protected by copyright. All rights reserved.

Author Manuscript

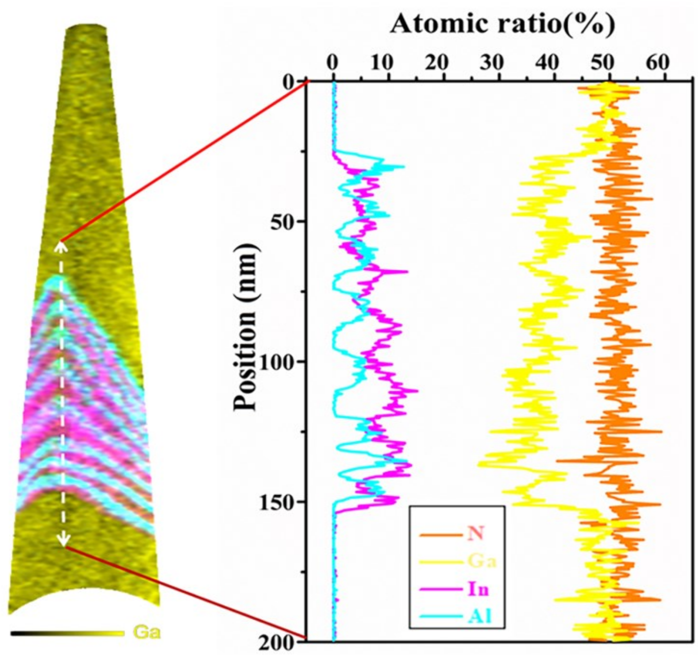

1 Introduction

Driven by the increasing needs for smaller footprint, higher light emission efficiency, and full-spectrum RGB light emission, semiconductor devices with desired properties are being widely explored [1]. Ternary III-N based nanorod (NR) heterostructures are known for their excellent light emitting stability and tunable color emission ability [2-6]. Especially, the light emission in the green light range is crucial for visible light communication, high-density optical information storage, full-color LED designs and so on [7,8]. Using In atoms to (partially) replace Ga atoms in GaN lattice, the bandgap of (In)GaN decreases from 3.30 eV to 0.65 eV [9,10], which could cover the whole region of visible light [6]. When including Al

This article is protected by copyright. All rights reserved.

Author Manuscript

atoms, the bandgap of (Al)GaN can increase from 3.30 eV to 6.06 eV [11]. Therefore, the elemental composition plays a significant role in modulating the light emission wavelengths of the nanorods. Furthermore, both axial and radial ternary III-N heterostructure configurations have been proposed [12-19]. The planar configuration of the ternary III-N heterostructures has been extensively studied for its simplicity, but it is generally limited by the difficulty in controlling defect density and strain effects [12-14]. The relatively large spontaneous polarization and piezoelectric field could adversely influence the performance of the devices. The radial heterostructures could largely reduce polarization fields. However, there are several obstacles hindering the development of radial devices: (1) The cost of m-plane substrates are usually expensive, increasing the costs of the devices; (2) The epitaxial growth of the heterostructures on the nonpolar planes will lead to poor crystal quality [15]; (3) They are restricted by achieving uniform current spreading, limiting the applications to single radial devices [16-18]. Therefore, it is important to explore novel structure design strategies for the ternary III-N heterostructures. Growing InGaN on a semipolar surface has been found to be an efficient way to increase the In content and reduce the defects [20, 21], while its nanoscale structure-property relationship remains largely unexplored. The spontaneous polarization direction of (In/Al)GaN is along [0001] in the wurtzite structure, the larger the slope of the facet the smaller the component of the polarization field perpendicular

This article is protected by copyright. All rights reserved.

Author Manuscript

to the facet [22-25]. Facets with larger slope display decreased quantum-confined Stark effect (QCSE) and thus could exhibit higher light emitting efficiency [21,26,27].

Selected-area molecular-beam epitaxy (MBE) growth has been demonstrated to be a controllable way of growing ternary III-N based nanorods in a bottom-up approach, which could dramatically reduce the number of defects (especially dislocations and/or stacking faults) [26,28, 29]. The nucleation of the nanowires from adatoms can be limited only to the exposed surface on the substrate leading to uniform morphology of the nanorods. Here, the GaN nanorods with sequential layers of "hollow hexagonal pyramid"-shaped InGaN/AlGaN QWs (InGaN/AlGaN@GaN NR) were synthesized by selected-area MBE [26]. The corresponding atomic structures and the three-dimensional morphology and composition were further characterized with scanning transmission electron microscopy (STEM) and atom probe tomography (APT). Combined with the cathodoluminescence (CL) spectroscopy measurement of the InGaN/AlGaN@GaN NR, the corresponding optical properties were successfully correlated with their composition and strain. Our results and combined strategy provide a new understanding of the light emission wavelengths based on the crystal structure and composition, and will contribute to the design and performance improvement of III-N-based LED.

This article is protected by copyright. All rights reserved.

Author Manuscript

2 Results and Discussions

Figure 1(a) presents a top-view SEM image of the vertically grown InGaN/AlGaN@GaN NRs which grow along the *c*-axis of GaN and possesses a hexagonal shape with six $\{10\bar{1}0\}$ side facets. The InGaN/AlGaN@GaN NR array exhibited a high degree of uniformity with a diameter of ~200 nm. Figure 1(b) shows a HAADF-STEM image of the cross-sectional sample extracted and thinned following Focused Ion Beam (FIB) milling (from the red framed region in Figure 1(a) and viewed along the $[2\bar{1}\bar{1}0]$ zone axis. From this projection, a “boomerang”-shaped QW region can be clearly observed within the GaN NR and a schematic illustration of the InGaN/AlGaN@GaN NR geometry can be found in Figure S1. A high-resolution HAADF-STEM image of the yellow framed region in Figure 1(b) is shown in Figure 1(c), where eight pairs of alternating InGaN/AlGaN layers can be clearly observed. For extremely thin III-Nitrides quantum wells and quantum disks, the quantum confinement effect is strong when the thickness is 1-3 atomic monolayers [30-35]. In our system, the thickness of each InGaN or AlGaN layers is measured to be 9 atomic monolayers or above, thick enough to neglect the spatial quantum confinement. Since the contrast of the HAADF-STEM images is highly dependent on the effective atomic number (Z), and elements with a higher Z appear brighter in the resulting image [36], InGaN layers are brighter than the neighboring AlGaN layers in the GaN NR.

This article is protected by copyright. All rights reserved.

Author Manuscript

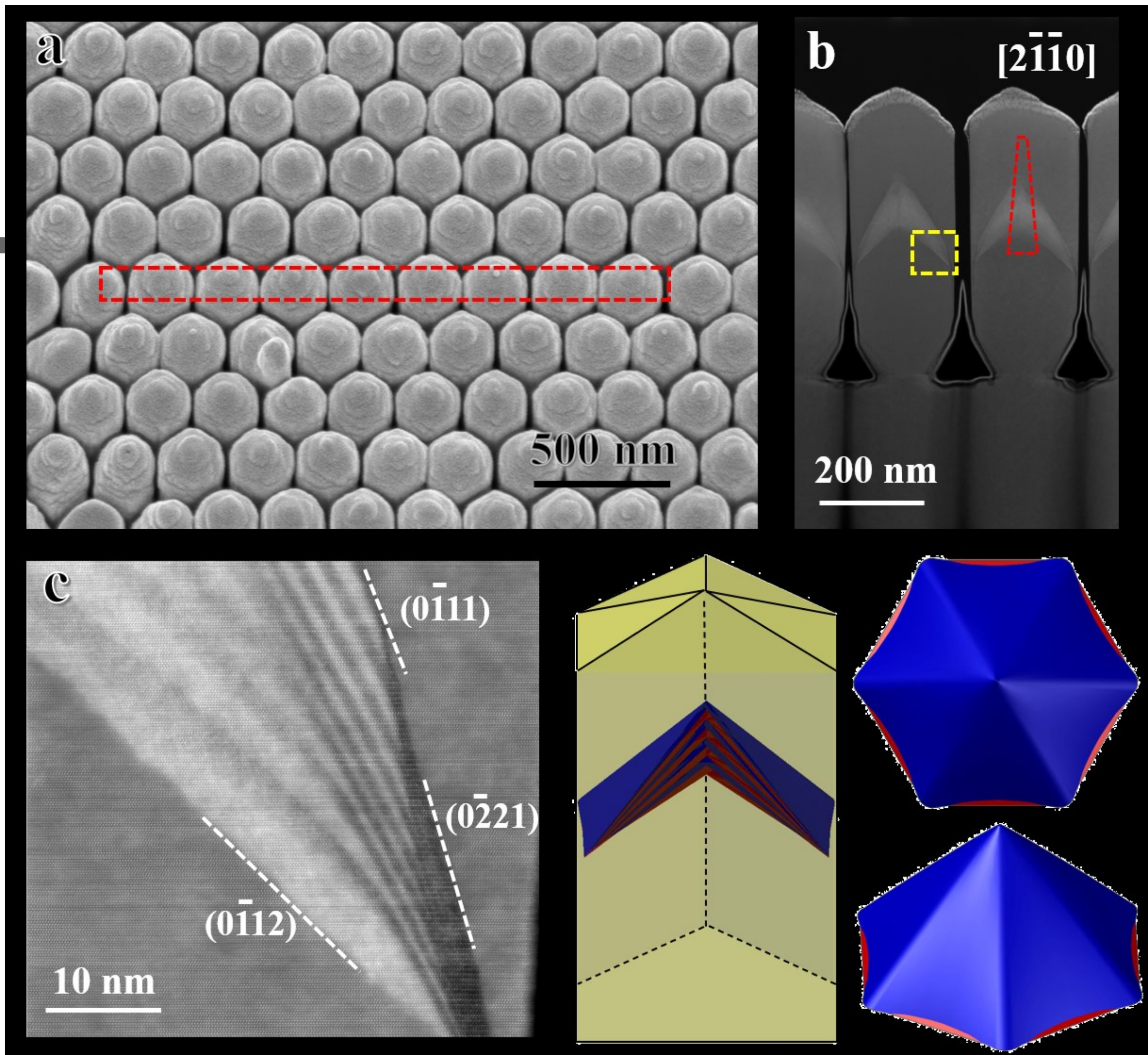

Figure 1. Electron microscopy characterization and schematic illustration of the InGaN/AlGaN QWs@GaN NR. (a) SEM image showing the top view of the NR. The red dashed rectangle indicate the FIB fabrication region. (b) Low magnification HAADF-STEM image of the FIB-fabricated cross-sectional sample viewed along the $[2\bar{1}\bar{1}0]$ zone axis. The area in the framed red triangle shows the position of the sample extracted for the atom probe

This article is protected by copyright. All rights reserved.

Author Manuscript

tomography experiments. (c) High resolution HAADF-STEM image of the yellow framed region in (b). (d) Schematic illustration of the InGaN/AlGaN QWs@GaN NR configuration. The GaN, InGaN, and AlGaN are shown in yellow, red and blue colors, respectively. Only four pairs of InGaN/AlGaN layers have been illustrated for simplicity. (e) The top-view and side-view of one pair of the InGaN/AlGaN QWs.

It should be mentioned that the interfaces of InGaN/AlGaN QWs evolves from the $(0\bar{1}12)$ plane into the $(0\bar{1}11)$ plane as shown in Figure 1(c), suggesting that the $(0\bar{1}12)$ plane is more energically stable and behaves as the growth front during the growth of GaN, while the $(0\bar{1}11)$ plane is the most energetically favorable plane for the InGaN/AlGaN growth. Due to different chemical potential for different facets, GaN shows growth-rate anisotropy [27,37]. A closer examination of the QWs revealed that the growth planes of InGaN/AlGaN evolved from $(0\bar{1}12)$ to $(0\bar{1}11)$ plane within 4 pairs of QWs from bottom to top. A schematic 3D illustration of the InGaN/AlGaN QWs@GaN NR is shown in Figure 1(d). In each InGaN and AlGaN layer, the growth planes converged to the same points at the bottom corners (Figure 1(c) and Figure S2), due to the fact the lateral growth is slower than axial growth. Compared with the planar configuration illustrated in Figure S2, the free carriers within InGaN functional layers can be better screened by the AlGaN layers all around

This article is protected by copyright. All rights reserved.

Author Manuscript

the InGaN structures in this "Russian Doll" hollow hexagonal pyramid shape (The sealing AlGaN structures are clearly visible in Figure 1(c)). The recombination of carriers with surface defects can be effectively avoided, which has the potential to boost the light-emission efficiency.

Then CL spectroscopy was performed to investigate the specific local optical properties of the synthesized InGaN/AlGaN QWs@GaN NR leading to direct information on the local optical response of such NRs as demonstrated in Figure 2 [38]. Figure 2(a) shows the HAADF-STEM image of the cross sectional view of the FIB sample, which was thinned down to one-nanorod thick (about 200 nm) at very low ion beam voltage (5 keV) in order to study the light emission performance of the whole InGaN/AlGaN QWs stack within the NR. The spatially resolved CL emission wavelengths mapping for the InGaN/AlGaN QWs, overlaid on the corresponding SEM image, is shown in Figure 2(b). The distribution of light follows the QWs shape and shows a range of colors. According to the CL spectra and colour maps, it is observed that the light emission range from 350 nm to 600 nm and the emission originates from different regions of the InGaN/AlGaN QWs. The CL spectra of the emitted light within the visible range extracted from four different positions (highlighted in Figure 2(b) with separate dots of different colours) are plotted in Figure 2(c). More spectra extracted from different areas can be found in the Supporting Information document. Since AlGaN possesses a larger bandgap than InGaN, the light emission in the visible range mainly comes

This article is protected by copyright. All rights reserved.

Author Manuscript

from the InGaN layers. The dot marked as Position 1 (the yellow dot and spectrum) at the bottom of the stack corresponding to the pure GaN region and the peak near 372 nm is a characteristic CL peak for bulk GaN [39,40]. Figure 2(d,e) show the CL line-scan results along the yellow and red arrows directions indicated in Figure 2(b), respectively. According to our CL measurement, it is found that the InGaN/AlGaN QWs mainly emit in the range of 510 nm to 538 nm (indicated by the green arrows in Figure 2(c), corresponding to green light).

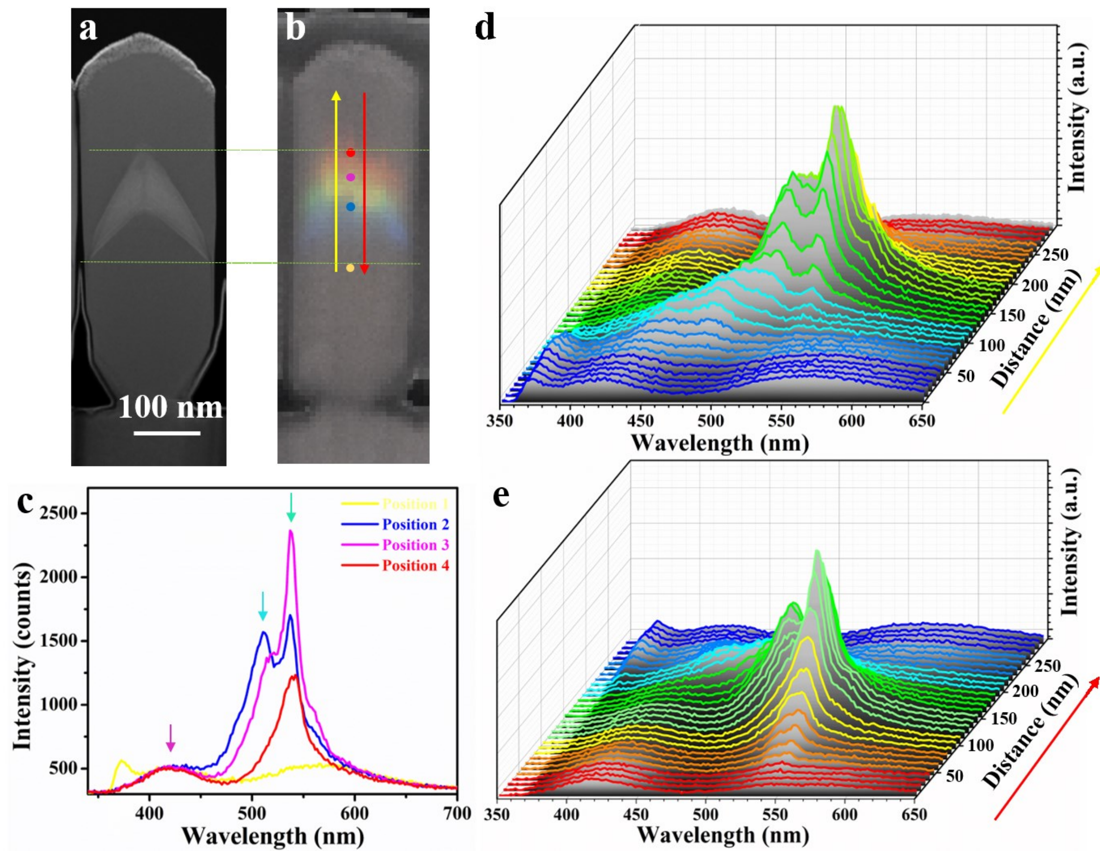

Figure 2. Cathodoluminescence (CL) analyses for InGaN/AlGaN QWs. (a) HAADF image for the QWs. (b) Spatially resolved CL mapping for the QWs overlayed on a SEM image of

This article is protected by copyright. All rights reserved.

the area scanned. The horizontal green dashed lines are used as the reference position between the CL mapping and HAADF image. (c) The CL spectra extracted from the dotted positions in (b). Spectrum for position 1 corresponding to the yellow dot position shown in (b) and located below the bottom of the stack while Spectrum for position 4 corresponds to the top of the stack and the red dot in (b). (d) The line scan CL results along the yellow arrow area in (b). (e) The line scan CL results along the red arrow area in (b).

Since the concentration of In in ternary III-N compounds can most effectively influence the band gap which directly determines emission properties, investigation of the three-dimensional composition distribution of the "boomerang"-shaped InGaN/AlGaN QWs is an absolute necessity for the understanding of its light emiting performance. However, characterization methods such electron energy loss spectroscopy (EELS) or energy dispersive X-ray spectroscopy (EDS), due to the integration of signals from projections, cannot directly extract 3D information about the composition distribution of the InGaN/AlGaN QWs with such a complex geometry. As an analytical method, APT has been proven to be an effective tool to provide 3D information of semiconductor materials with complex morphology, structure and composition distributions [41-43]. Therefore, the APT technique is applied here to directly reveal the 3D composition distribution of the InGaN/AlGaN QWs. As shown in

Author Manuscript

This article is protected by copyright. All rights reserved.

Figure 3(a), a needle-like InGaN/AlGaN QWs@GaN sample fabricated from the red framed region in Figure 1(b) was used for the APT measurement. The atomic composition maps for In, Al, In&Al and In&Al&Ga are presented in Figure 3(a), from which we can find that the Al rich layers (AlGaN) are well separated and sharp while the In layers (InGaN) are relatively smeared out. This might be caused by the relatively higher mobility of In than Al during the synthesis process [44]. The atomic ratios of the Al, In, Ga and N elements are presented in Figure 3(b), from which eight atomic ratio peaks of In and Al can be observed, corresponding to the eight pairs of InGaN/AlGaN QWs. As expected, the atomic ratio of N was measured to be 50% both in the GaN, and across the InGaN/AlGaN QWs (Figure 3(b)).

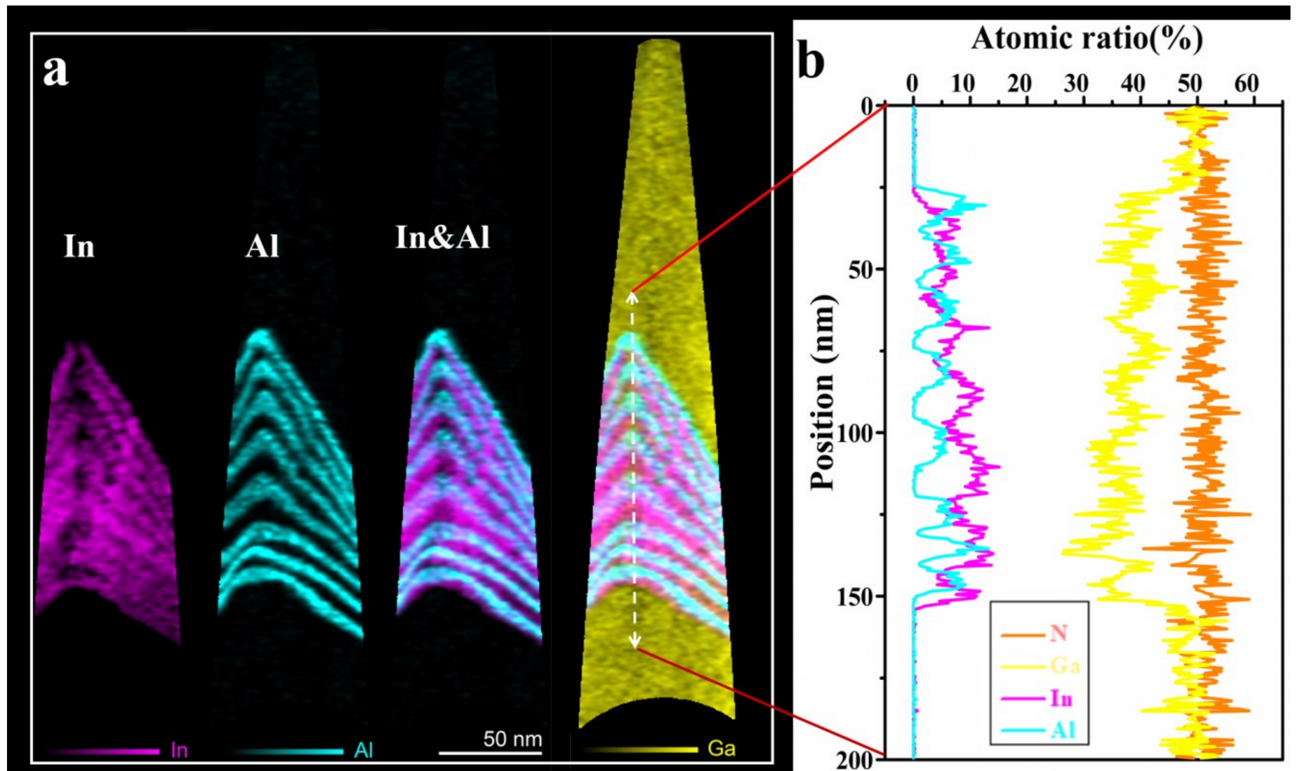

This article is protected by copyright. All rights reserved.

Author Manuscript

Author Manuscript

Figure 3. Concentration maps of In, Al, Ga taken from a 5 nm thick subsection of the nanorod APT data. (a) The concentration of In, Al, In & Al, and Ga (from left to right). The colour bars represent the relative amounts of each element. (b) The atomic ratio for each element across the QWs.

Accompanied with detailed analyses of the composition distribution, the detailed 3D morphology of InGaN/AlGaN QWs can also be demonstrated in APT. As shown in Figure S4 and S5, the top AlGaN facet is flat, while the bottom facet exhibits a curved morphology. The curved facet evolves between the $(0\bar{1}11)$ plane and the $(0\bar{1}12)$ plane, because $(0\bar{1}11)$ and $(0\bar{1}12)$ are the most energetically favourable planes for the growth of AlGaN and GaN respectively[45,46]. As shown in Figure 1(c), it is important to mention that the intensity of the bottom four AlGaN layers is relatively weaker compared with the intensity of the top four AlGaN layers and that the apparent width of the layer is also larger for the bottom InGaN dots than the top ones, all factors which can be explained by the curved nature of the bottom AlGaN layers. Given the complex nature of this heterostructure, it is clear that the combination of APT technique with the information from TEM are the the only combined approaches that can reveal this slightly curved nature of the quantum layers and the crystallographic nanosized structure within the heterostructures.

This article is protected by copyright. All rights reserved.

Author Manuscript

In order to provide a better understanding on the light emission behavior of the InGaN/AlGaN QWs@GaN NRs, calculations based on k·p theory in which important materials parameters were obtained from DFT results, were further utilized to elucidate the band structure modulation due to In incorporation and the strain effects. First of all, without considering strain effects, the evolution of light emission of GaN with different concentrations of In and Al is shown in Figure S7(a). The light emission can be tuned from the ultraviolet to visible light with increasing In doping levels. Equally important, the results of our calculation show that the InGaN could achieve full-visible-light emission with different In concentrations. According to the light emission spectra (Figure 2), three compounds corresponding to the three CL peaks (marked by arrows) should appear within InGaN layers. Considering the fact that atomic concentration maps of each element acquired from APT (Figure 3(b)) cannot directly reflect the CL light emission property and the light emission spectra (Figure 2), we used a linear combination method to inversely retrieve the relative fractions for each InGaN compound in the NR. The relative fractions of three InGaN compounds in the nanorod are quantitatively obtained and plotted in Figure S7(b). With respect to AlGaN in this NR, this compound will not contribute to the visible-light emission. Alternatively, AlGaN acts as the confinement layer for the recombination of the excitons as discussed above.

This article is protected by copyright. All rights reserved.

Author Manuscript

It should be mentioned that, as displayed in Figure 1(c), InGaN and AlGaN layers are grown alternating. InGaN layers will inevitably experience biaxial stress induced by the lattice mismatch, typically, $(0\bar{1}12)$, $(0\bar{1}11)$ and $(0\bar{2}21)$ planes as depicted in Figure 1(c). The different factes will have different influence on the properties[47,48]. Through the use of the $K \cdot P$ perturbation approach and deformation potential theory [49] (See details in the Supporting Information), we calculated the biaxial strain effect on the light emission spectra of $In_xGa_{1-x}N$. Since the strain components vary depending on which crystal plane the InGaN was grown, three light emission wavelength evolution graphs along with different In concentrations of $In_xGa_{1-x}N$ grown on $(0\bar{2}21)$, $(0\bar{1}11)$ and $(0\bar{1}12)$ planes are presented in Figure 4(a) and Figure S8. The detailed strain components and bandgap changes brought by these biaxial stresses for different $In_xGa_{1-x}N$ compounds with various In content x are summarized in Table S1. Considering the fact that CL spectra were acquired from the whole QWs (the sample thickness for CL tests was about 200 nm), the strain effects from these three energy favorable planes are considered. Then, relative fraction of the three InGaN compounds of the nanorod calculated from averaged strain components over different growth planes, *i.e.* $(0\bar{2}21)$, $(0\bar{1}11)$ and $(0\bar{1}12)$, are quantitatively obtained and plotted in Figure 4b. For InGaN, there are three different compounds existing in the nanorod. They are $In_{0.10}Ga_{0.90}N$, $In_{0.27}Ga_{0.73}N$ and $In_{0.31}Ga_{0.69}N$, whose bandgap are 2.97 eV, 2.43 eV and 2.31 eV, corresponding to light emission wavelength of 418 nm, 510 nm and 538 nm, respectively.

This article is protected by copyright. All rights reserved.

It should be mentioned that $In_{0.27}Ga_{0.73}N$ and $In_{0.31}Ga_{0.69}N$ will contribute to green light emission, and they are the main compositions of the nanorod. Comparing the results with (Figure 4(b)) and without (Figure S7(b)) strain effects, we find the strain will modify the effective components. Taking the broadening of the light emission spectrum peaks into consideration, blue-green-yellow emission could be achieved in these NRs. The broadening of the peak is mainly related to the broadening of the valence band maximum and conduction band minimum in $In_xGa_{1-x}N$, and the compositional fluctuation of the elements across the QWs.

Author Manuscript

This article is protected by copyright. All rights reserved.

Author Manuscript

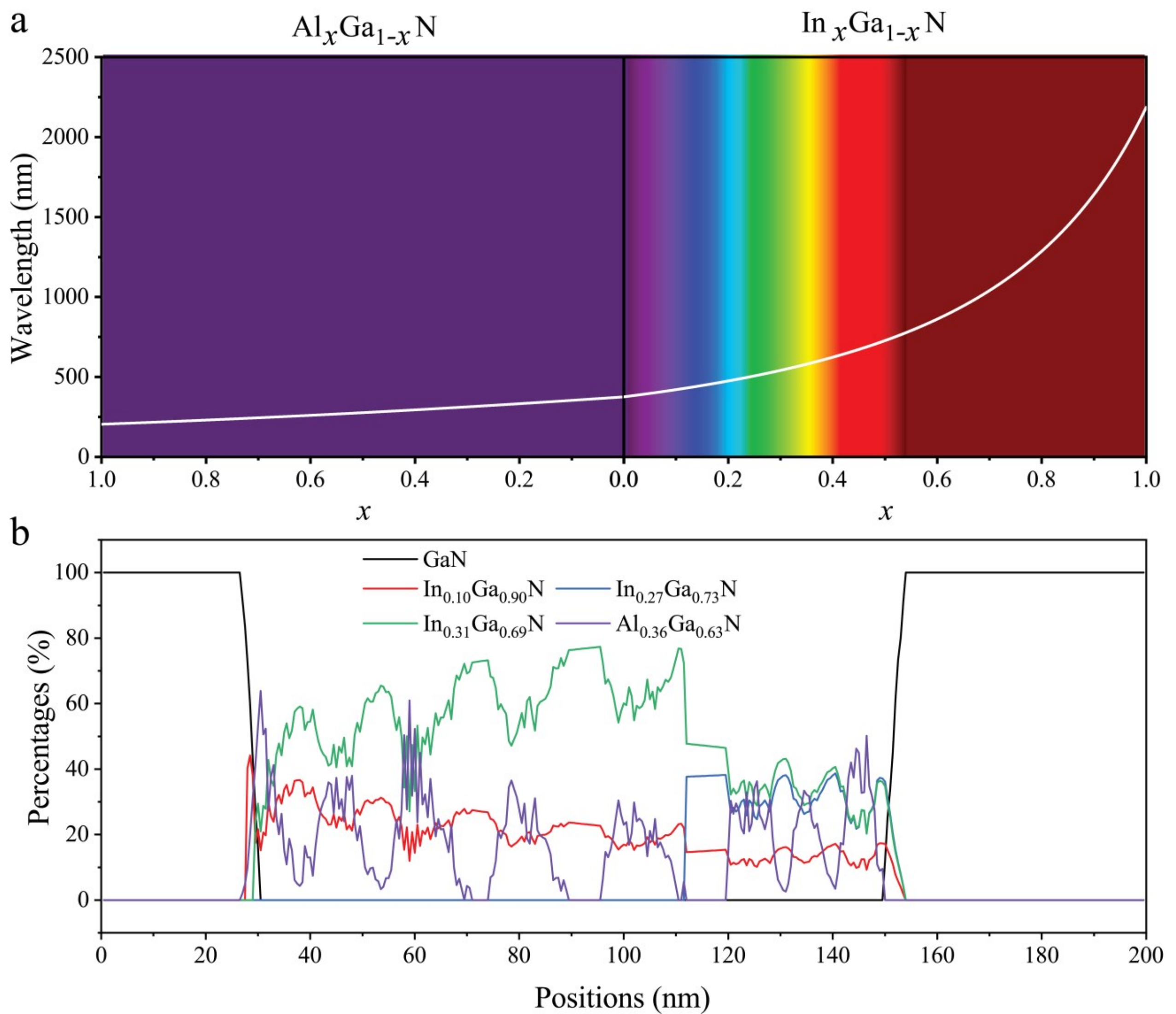

Figure 4. Calculated light emission and nanorod compositions analyses. (a) Light emission wavelength evolution in $Al_xGa_{1-x}N$ and $In_xGa_{1-x}N$ where biaxial stress induced by the lattice mismatch between InGaN ($0\bar{2}21$) and AlGaN ($0\bar{2}21$) are taken into consideration. Infrared light is marked as dark red (rightmost), and ultraviolet light is marked as dark purple (leftmost). The white curve depicts the wavelength of light

This article is protected by copyright. All rights reserved.

Author Manuscript

emission spectra peak evolution along with different concentrations. (b) The percentage distributions of different compounds in the nanorod along the [0001] pole. The chemical formula of InGaNs are obtained from the averaged strain components. X-axis the same as the Y-axis in Figure 3(b).

Additionally, all the interfacial planes in the featured region of the NR are semipolar ones in the III-Nitrides (Figure 1(c)). Compared with the polar *c*-plane which has an estimated polarization field strength 0.042 C/m^2, the polarization fields are estimated to be in the range of 0.000~0.004 C/m^2 in the semipolar InGaN/AlGaN QWs (SQWs), essentially close to zero which is the value for nonpolar QWs. In these conditions the carrier overlap is increased [50,51], leading to enhanced performance of light emitting in SQWs. On the other hand, as plotted in Figure S9, the transition energy change, E_3 (Equation (3) in the Supporting Information for more details), which determines the strain-induced bandgap change of InGaN, is always much smaller in SQWs than that in the nonpolar InGaN/AlGaN QWs. This means that, for a given x in $In_xGa_{1-x}N$, SQWs always have a smaller bandgap, helping with the green-light-emission. With the observed curved nature of AlGaN, the effect on the light emission properties of the nanorods can be estimated based on the above analysis of the strain-induced transition energy changes as well as the influence of polarization fields

This article is protected by copyright. All rights reserved.

Author Manuscript

existing on different III-Nitrides planes. The facets with large slope have small polarization field. Consequently, facets with larger slope exhibit higher light emitting efficiency. Secondly, facets with small slope will be favorable for achieving the challenging light emission within the long wavelength region, such as green or even red-light emission, which is due to the smaller transition energy changes. Therefore, our findings provides a useful guidance for the structure design of InGaN based optical device.

3 Conclusions

Using a combination of transmission electron microscopy, atom probe tomography, cathodoluminescence spectroscopy, and k·p theory calculations, we have elucidated the structure and properties relationships of these “Russian Doll”-type InGaN/AlGaN QWs. A new three-dimensional design for the quantum heterostructures by selective-area molecular-beam epitaxy method has been demonstrated, achieving green light emission. Their structure, with growth on semi-polar planes, could efficiently reduce the defects and strain effects compared with traditional planar design of ternary III-N heterostructures. More insights have been provided for understanding the behavior of light emission within the quantum wells. This work provides a new route for robust, transferable 3D-nanoscale optical and structural analyses in modern nanoscale materials and devices.

This article is protected by copyright. All rights reserved.

Author Manuscript

Experimental Section

Sample fabrication. Zeiss NVision 40 (Carl Zeiss, Germany) dual-beam focused ion beam (FIB) system was used to prepare samples for the TEM, APT and CL characterization, with the low-voltage ion beam at 5 kV as the final step for reducing/removing the surface damage layers. The schematic diagram of the sample configuration can be found in the Supporting Information. It should be mentioned the thinner lamellae (less than one-nanorod thick) for CL tests clearly behaved differently suggesting that the material and or carrier behavior was altered.

Characterization. The TEM studies were carried out using a FEI Titan 80/300 TEM equipped with a high-resolution electron energy-loss spectrometer (Gatan Imaging Filter (GIF) model 966) and a state-of-the-art Gatan K2 Summit direct electron detector (K2 IS). The high-angle annular dark-field scanning transmission electron microscopy (HAADF-STEM) images and spectrum images were acquired at 200 kV with a convergence semi-angle of 19 mrad and a GIF collection semi-angle of 20.7 mrad. The dwell time of the energy-loss spectroscopy (EELS) mapping was set to 30 ms to increase the mapping area and minimize the beam damage. The SEM images were captured with a ThermoFisher Scientific G4 Plasma FIB equipped with a monochromated Elstar SEM column. The secondary electron

This article is protected by copyright. All rights reserved.

Author Manuscript

image was then collected by using a Through Lens detector (TLD) at 25 pA , 1 kV under immersion mode, with monochromator on.

The APT analyses were performed using a Cameca Instruments LEAP 4000X HR operating in laser-pulsing mode (λ = 355 nm) with a pulse energy of 50 fJ and a pulse rate of 100 kHz. A target detection rate of 1% (0.01 ions/pulse) was maintained for evaporation by controlling the DC voltage applied to the sample, which varied between ~3 and 6 kV. The specimen were held at a base temperature of approximately 38 K. Data reconstruction and analysis was performed using IVAS 3.8.2, with SEM images of the samples and plane-spacing measurements of $(0001)_{GaN}$ used to spatially-calibrate the reconstruction.

CL spectroscopy was performed using a SPARC CL detection system mounted on a Thermo Fisher Quanta 650 field emission gun Scanning Electron Microscope [52]. The SPARC system is equipped with a back-illuminated Peltier-cooled CCD camera mounted on a Czerny Turner spectrograph. Hyperspectral CL imaging was performed using a 300 lines/mm ruled diffraction grating, blazed for a wavelength of 500 nm. The CL emitted from the sample is collected using an aluminium parabolic mirror with an acceptance angle of 1.49π sr, aligned with respect to the sample using a motorised stage. Spatial CL imaging was performed at 30 keV and beam current of 45 pA. These beam conditions gave the most stable and high-resolution imaging results, while maintaining an adequate signal-to-noise ratio.

This article is protected by copyright. All rights reserved.

Author Manuscript

ASSOCIATED CONTENT

Supporting information

The following files are available free of charge.

The detailed strain analyses, schematic diagrams showing the configurations of the nanorods, the sample preparation for the APT experiments. (file type, PDF)

AUTHOR INFORMATION

Conflicts of interest

Toon Coenen and Sangeetha Hari work for Delmic BV, the company that develops, manufactures and sells the SPARC CL system used in this work.

Author contributions

S. C. conceived and designed the experiments under the supervision of G.A.B.. S.C., A.P., H.Y. X.L. conducted the TEM and SEM experiments. Z.W., X. K. and H. G. performed the simulations. B.L. conducted APT experiments. T.C. and S.H. carried out CL measurement.

This article is protected by copyright. All rights reserved.

Author Manuscript

Y.-H. R., R.T.R., and Z.M. designed and grew the samples. S.C., Z.W., and X. K. co-wrote the paper with all the authors contributing the discussion and preparation of the manuscript.

Acknowledgement

S. C and Z. W contributed equally to this work. G. A. B and S. C. are grateful to NSERC for a Discovery Grant partially supporting this work. G. A. B. and Z. M. acknowledge partial support from a Strategic Project Grant. Z. M. would like to acknowledge National Science Foundation (Grant ECCS-1709207). Electron microscopy was carried out at the Canadian Centre for Electron Microscopy (CCEM), a national facility supported by NSERC, the Canada Foundation for Innovation, under the MSI program, and McMaster University. CL measurements were performed at NWO institute AMOLF (Amsterdam), a Dutch laboratory for fundamental science. H. G. acknowledge financial support of the Natural Science and Engineering Research Council of Canada, Emissions Reduction Alberta, and thank Compute Canada and the High Performance Computing Center of McGill University for computation facilities.

This article is protected by copyright. All rights reserved.

References

[1] S. Pimputkar, J. S. Speck, S. P. DenBaars, S. Nakamura, *Nat. Photonics* **2009**, *3*, 180.

[2] Y. H. Ra, R. Navamathavan, H. I. Yoo, C. R. Lee, *Nano Lett.* **2014**, *14,* 1537.

[3] F. Qian, Y. Li, S. Gradečak, D. Wang, C. J. Barrelet, C. M. Lieber, *Nano Lett.* **2004**, *4*, 1975.

[4] H. P. T. Nguyen, S. Zhang, A. T. Connie, M. G. Kibria, Q. Wang, I. Shih, Z. Mi, *Nano Lett.* **2013**, *13,* 5437.

[5] Y. H. Ra, R. Navamathavan, J. H. Park, C. R. Lee, *Nano Lett.* **2013**, *13,* 3506.

[6] T. Kuykendall, P. Ulrich, S. Aloni, P. Yang, *Nat. Mater.* **2007**, *6*, 951-956.

[7] F. A. Ponce, D. P. Bour, *Nature* **1997**, *386,* 351.

[8] Y. J. Zhao, H. Q. Fu, G. T. Wang, S. J. Nakamura, *Adv. Opt. Photonics* 2**018**, *10,* 246-308.

[9] M. César, Y. Ke, W. Ji, H. Guo, Z. Mi, *Appl. Phys. Lett.* **2011**, *98,* 202107.

[10] S. Zhao, S. Fathololoumi, K. H. Bevan, D. P. Liu, M. G. Kibria, Q. Li, G. T. Wang, H. Guo, Z. Mi, *Nano Lett.* **2012**, *12*, 2877.

Author Manuscript

This article is protected by copyright. All rights reserved.

Author Manuscript

[11] R. R. Pelá, C. Caetano, M. Marques, L. G. Gerreira, J. Furthmüller, L. K. Teles, *Appl. Phys. Lett.* **2011**, *98*, 151907.

[12] S. Y. Woo, N. Gauquelin, H. P. T. Nguyen, Z. Mi, G. A. Botton, *Nanotechnology* **2015**, *26,* 344002.

[13] T. Kehagias, *Nanotechnology* **2013**, *24*, 435702.

[14] S. M. Sadaf, Y. -H. Ra, H. P. T. Nguyen, M. Djavid, Z. Mi, *Nano Lett.* **2015**, *15,* 6696.

[15] B. O. Jung, S. -Y. Bae, S. Lee, S. Y. Kim, J. Y. Lee, Y. Honda, H. Amano, *Nanoscale Res. Lett.* **2016**, *11*, 215

[16] F. Qian, Y. Li, S. Gradečak, D. Wang, C. J. Barrelet, C. M. Lieber, *Nano Lett.* **2004**, *4*, 1975-1979

[17] S. -Y. Bae, J. -W. Min, H. -Y. Hwang, K. Lekhal, H. -J. Lee, Y. -D. Jho, D. -S. Lee, Y. -T. Lee, N. Ikarashi, Y. Honda, H. Amano, *Sci. Rep.* **2017**, *7*, 45345.

[18] B. O. Jung, S. -Y. Bae, S. Y. Kim, S. Lee, J. Y. Lee, D. -S. Lee, Y. Kato, Y. Honda, H. Amano, *Nano Energy* **2015**, *11*, 294-303

[19] T. R. Kuykendall, A. M. Schwartzberg, S. Aloni, *Adv. Mater.* **2015**, *27*, 5805-5812

This article is protected by copyright. All rights reserved.

Author Manuscript

[20] D. D. Koleske, S. R. Lee, M. H. Crawford, M. E. Coltrin, P. T. Fini, *Sandia Report* URL: https://prod-ng.sandia.gov/techlib-noauth/access-control.cgi/2013/135065.pdf **2013**.

[21] J. E. Northrup, *Appl. Phys. Lett.* **2009**, *95* 133107.

[22] F. Bernardini, V. Fiorentini, D. Vanderbilt, *Phys. Rev. B* **1997**, *56,* R10024(R).

[23] A. E. Romanov, T. J. Baker, S. Nakamura, J. S. Speck, *J. Appl. Phys.* **2006**, *100*. 023522.

[24] T. Wenicke, L. Schade, C. Netzel, J. Rass, V. Hoffmann, S. Ploch, A. Knauer, M. Weyers, Ul. Schwarz, M. Kneissl, *Semicond. Sci. Technol.* **2012**, *27*, 024014.

[25] Y. Zhao, R. M. Farrell. Y. -R. Wu, J. S. Speck, *Jpn. J. Appl. Phys.* **2014**, *53*, 100206.

[26] Y.-H. Ra, R. T. Rashid, X. Liu, J. Lee, Z. Mi, *Adv. Funct. Mater.* **2017**, *27,* 1702364.[27] S. Cheng, B. Langelier, Y. -H. Ra, R. T. Rashid, Z. Mi, G. A. Botton, *Nanoscale* **2019**, *11*, 8994.

[28] X. Li, M. Sun, X. Wei, C. Shan, Q. Chen, *Nanomaterials* **2018**, *8*, 188.

[29] M. Sun, X. Li, Z. Tang, X. Wei, Q. Chen, *Nanoscale* **2018**, *10*, 19733.

[30] G. Sarwar, B. J. May, M. F. Chisholm, G. J. Duscher, R. C. Myers, *Nanoscale* **2016**, *8*, 8024-8032

This article is protected by copyright. All rights reserved.

Author Manuscript

[31] D. Bayyerl, S. M. Islam, C. M. Jones, V. Protasenko, D. Jena, E. Kioupakis, *Appl. Phys. Lett.* **2016**, *109*, 241102.

[32] D. Bayyerl, E. Kioupakis, *Appl. Phys. Lett.* **2019**, *115*, 131101.

[33] A. Aiello, Y. Wu, A. Pandey, P. Wang, W. Lee, D. Bayerl, N. Sanders, Z. Deng, J. Gim, K. Sum, R. Hovden, E. Kioupakis, Z. Mi, P. Bhattchrya, *Nano Lett.* **2019**, *19*, 7852-7858.

[34] A. A. Toropov, E. A. Evropeitsev, M. O. Nestoklon, D. S. Smirnov, T. V. Shubina, W. Kh. Kaibyshev, G. V. Budkin, V. N. Jmerik. D. V. Nechaev, S. Rouvimov, S. V. Ivanov, B. Gil, *Nano Lett*. **2020**, *20*, 158-165.

[35] J. Sellés, C. Brimont, G. Cassabois1, P. Valvin, T. Guillet, I. Roland, Y. Zeng, X. Checoury, P. Boucaud, M. Mexis, F. Semond, B. Gayral, *Sci. Rep.* **2016**, *6*, 21650.

[36] S. Cheng, C. Xu, S. Deng, M. -G. Han, S. Bao, J. Ma, C. Nan, W. Duan, L. Bellaiche, Y. Zhu, J. Zhu, *Sci. Adv.* **2018**, *4*, eaar4298.

[37] G. Biasiol, E. Kapon, *Phys. Rev. Lett.* **1998**, *81*, 2962.

[38] S. Meuret, T. Coenen, S. Y. Woo, Y. -H. Ra, Z. Mi, A. Polman, *Nano Lett.* **2018**, *18*, 2288.

This article is protected by copyright. All rights reserved.

Author Manuscript

[39] M. Müller, P. Veit, F. F. Krause, T. Schimpke, S. Metzner, F. Bertram, T. Mehrtens, K. Müller-Caspary, A. Avramescu, M. Strassburg, A. Rosenauer, J. Christen, *Nano Lett.* **2016**, *16*, 5340.

[40] E. Kheirandish, N. A. Kouklin, J. Liang, *J. Nanomaterials* **2018**, 208, 5684150.

[41] L. Rigutti, I. Blum, D. Shinde, D. Hernández-Maldonado, W. Lefebvre, J. Houard, F. Vurpillot, A. Vella, M. Tchernycheva, C. Durand, J. Eymery, B. Deconihout, *Nano Lett.* **2014**, *14*, 107.

[42] J. R. Riley, S. Padalkar, Q. Li, P. Lu, D. D. Koleske, J. J. Wierer, G. T. Wang, L. J. Lauhon, *Nano Lett.* **2013**, 13, 4317.

[43] L. Rigutti, *Acta Phys. Pol. A* **2016**, *129*, A-7.

[44] S. Y. Woo, M. Bugnet, H. P. T. Nguyen, Z. Mi, G. A. Botton, *Nano Lett.* **2015**, *15*, 6413.

[45] Y. Tian, J. Yan, Y. Zhang, Y. Zhang, X. Chen, Y. Guo, J. Wang, J. Li, *Nanoscale* **2016**, *8*, 11012.

[46] H. Kum, H. -K. Seong, W. Lim, D. Chun, Y. -i. Kim, Y. Park, G. Yoo, *Sci. Rep.* **2017**, *7*, 40893.

This article is protected by copyright. All rights reserved.

Author Manuscript

[47] S. Hwang, N. Han, H. Jeong, J. H. Park, S. -H. Lim, J. -H. Cho, Y. -H. Cho, H. J. Jeong, M. S. Jeong, J. K. Kim, *Cryst. Growth Des*. **2017**, *17*, 3649-3655

[48] M. Sun, B. Yu, M. Hong, Z. Li, F. Lyu, X. Li, Z. Li, X. Wei, Z. Zhang, Y. Zhang, Q. Chen, *Small* **2020**, *16*, 1906435

[49] J. Bardeen, W. Shockley, *Phys. Rev.* **1950**, *80*, 72.

[50] B. A. Haskell, F. Wu, S. Matsuda, J. S. Speck, *Appl. Phys. Lett.* **2003**, *83*, 1554.

[51] A. Tyagi, Y. -D. Lin, D. A. Cohen, M. Saito, K. Fujito, J. S. Speck, S. P. DenBaars, S. Nakamura, *Appl. Phys. Express* **2008**, *1*, 091103.

[52] T. Coenen, S. V. D. Hoedt, A. Polman, *Micros Today* **2016**, *24*, 12.

[53] Q. Yan, P. Rinke, A. Janotti, M. Scheffler, C. G. Van de Walle, *Phys. Rev. B* **2014**, *90*, 125118.

[54] Q. Yan, P. Rinke, M. Scheffler, C. G. Van de Walle, *Appl. Phys. Lett.* **2010**, *97*, 181102.

[55] A. E. Romanov, T. J. Baker, S. Nakamura, J. S. Speck, *J. Appl. Phys.* **2006**, *100*, 023522.

[56] A. F. Wright, *J. Appl. Phys.* **1997**, *82*, 2833.

This article is protected by copyright. All rights reserved.